Thermal and mechanical stability of wurtzite-ZrAlN/cubic-TiN and wurtzite-ZrAlN/cubic-ZrN multilayers

Y.H. Chen[1*], L. Rogstro□m[1], J.J. Roa[2], J.Q. Zhu[1], I. C. Schramm[1,3], L.J.S. Johnson[4], N. Schell[5], F. Mücklich[3], M.J. Anglada[2] and M. Odén[1]

[1] Nanostructured Materials, Department of Physics, Chemistry and Biology (IFM), Linköping University, SE-581 83 Linköping, Sweden

[2] Departament de Ciència dels Materials i Enginyería Metal·lúrgica, Universitat Politècnica de Catalunya, EEBE-Campues diagonal Besòs, 08019 Barcelona, Spain

[3] Functional Materials, Department of Materials Science, Campus D3.3, Saarland University, D 66123 Saarbrücken, Germany

[4] Sandvik Coromant, SE-126 80 Stockholm, Sweden

[5] Helmholtz-Zentrum Geesthacht (HZG), Max-Planck-Str. 1, D-21502 Geesthacht, Germany

* Corresponding author: yuhch@ifm.liu.se

Abstract

The phase stability and mechanical properties of wurtzite (*w*)-$Zr_{0.25}Al_{0.75}N$/cubic (*c*)-TiN and *w*-$Zr_{0.25}Al_{0.75}N$/*c*-ZrN multilayers grown by arc evaporation are studied. Coherent interfaces with an orientation relation of *c*-TiN (111)[1-10]‖ *w*-ZrAlN (0001)[11-20] form between ZrAlN and TiN sublayers during growth of the *w*-ZrAlN/*c*-TiN multilayer. During annealing at 1100 °C a *c*-Ti(Zr)N phase forms at interfaces between ZrAlN and TiN, which reduces the lattice mismatch so that the coherency and the compressive strain are partially retained, resulting in an increased hardness (32 GPa) after annealing. For the *w*-ZrAlN/*c*-ZrN multilayer, there is no coherency between sublayers leading to strain relaxation during annealing causing the hardness to drop. The retained coherency between layers and the compressive strain in the *w*-ZrAlN/*c*-TiN multilayer results in superior fracture toughness compared to the *w*-ZrAlN/*c*-ZrN multilayer as revealed by cross-sectional investigations of damage events under scratch and indentation tests.

Keywords: Multilayers; ZrAlN coatings; Scratch test; Fracture toughness; Arc evaporation

1. Introduction

Wear resistance of protective coatings at high temperature is critical for cutting and machining tools [1], where the operating temperature may exceed 1000 °C [2]. One way to achieve high thermal stability and good mechanical properties is to design an alloy that decomposes at high temperature into a nanocomposite and exhibits age hardening [3, 4]. The archetype for this approach is the metastable cubic (*c*-) $Ti_{1-x}Al_xN$ solid solution, which forms nm-sized domains by spinodal decomposition when exposed to high temperatures (around 900 °C) [5-8]. At even higher temperatures this alloy further decomposes into its thermodynamically stable phases *c*-TiN and wurtzite (*w*-) AlN [9] that deteriorates the mechanical properties [10, 11]. The related $Zr_{1-x}Al_xN$ alloys display characteristics similar to $Ti_{1-x}Al_xN$ with a miscibility gap for cubic solid solutions and a higher driving force for decomposition compared to $Ti_{1-x}Al_xN$ [12, 13] resulting in promising mechanical properties [14-18] at high temperature. In addition to cubic solid solutions, wurtzite structured $Zr_{1-x}Al_xN$ solid solutions have high thermal stability when the Al content is higher than ~70% [13]. It has also been shown to exhibit spinodal decomposition at high temperature [19] resulting in good wear behavior during cutting applications [20].

Multilayered structures incorporating hard coating materials can be designed to improve the thermal stability [21-23], mechanical properties [24, 25] and wear behavior [26, 27]. For example, when sandwiching ZrAlN and TiN during very high temperature (900 °C) growth conditions, the multilayer architecture allows for growth of *c*-AlN in a *c*-ZrN matrix in the ZrAlN sublayers where *c*-AlN further transforms to *w*-AlN when exposed to mechanical stress [28]. The transformation is associated with a volume expansion that promotes crack closure and yields an enhanced fracture toughness of the coatings [27, 29]. Promising data has also been reported for low Al content *c*-ZrAlN/TiN multilayers grown at more moderate temperatures (400 °C) displaying superior hardness at 1100 °C compared

with ZrAlN and TiAlN single layers; ZrAlN/ZrN and TiAlN/TiN multilayers [30]. The enhanced hardness is suggested to be an effect of the secondary phase, *c*-ZrTi(Al)N, formed during annealing. In addition, tribological tests of cohesion/adhesion and wear resistance have demonstrated the enhancement of such properties from multilayered structures [26, 27, 31].

In this study, we use the multilayer design and combine high Al-content (~75%) *w*-ZrAlN with high thermal stability with a stable *c*-TiN or *c*-ZrN phase. We grow *w*-ZrAlN/*c*-TiN and *w*-ZrAlN/*c*-ZrN multilayer coatings by cathodic arc evaporation and report their microstructure evolution and thermal stability and its effect on the mechanical properties. A secondary phase, *c*-Ti(Zr)N, forms at the interfaces in the *w*-ZrAlN/*c*-TiN multilayers during annealing which stabilizes the coherent interfaces between *w*-ZrAlN and the cubic phase, leading to sustained compressive strain and an enhanced hardness and crack resistance.

2. Experimental details

w-$Zr_{0.25}Al_{0.75}N$/*c*-TiN and *w*-$Zr_{0.25}Al_{0.75}N$/*c*-ZrN multilayer coatings were deposited by cathodic arc evaporation in an Oerlikon Balzers Innova system on polished cemented carbide (WC-Co) substrates (12 × 12 mm^2). Deposition of multilayer coatings was performed by placing a $Zr_{17}Al_{83}$ cathode and a Ti or Zr cathode on each side of the chamber. The polished WC-Co substrates were placed on a rotating fixture (single rotation) rotating with 2.5 rpm. The depositions were performed at a total pressure of 1.6 Pa in a mixed flow of N_2 (400 sccm) and Ar (200 sccm), a substrate temperature of 400 °C, and a substrate bias of -30 V. With this growth condition, two multilayer coatings with a similar bilayer period of ~15 nm consisting of ~10 nm of TiN (ZrN) and ~5 nm of ZrAlN are resulted. Total thickness of the coating is ~5 µm and ~6 µm for TiN and ZrN multilayers respectively, which is measured

on cross-sections of the coating carried out by focused ion beam (FIB) milling (Zeiss, Neon 40). The difference in their total thickness is a result from the difference in deposition rate between ZrN and TiN. The alloy composition of ZrAlN was determined from the *w*-ZrAlN/*c*-TiN sample by energy-dispersive x-ray spectroscopy (EDS) in a Leo 1550 Gemini SEM operated at 20 kV, and we assume that the composition is the same for the *w*-ZrAlN/*c*-ZrN sample.

In situ wide angle x-ray scattering (WAXS) experiments during annealing were carried out at beamline P07 (high-energy materials science beam line) at PETRA III, DESY in Hamburg using a 75 keV (λ=0.165 Å) x-ray beam with a size defined to 500×20 μm^2 using slits. The WAXS signal was recorded from a 1 mm thick cross-sectional slice cut from the coated substrate using transmission geometry. The thermal annealing was performed in a vacuum chamber with a work pressure of 1.6 mPa at an isothermal annealing temperature of 1100 °C for approximately 2 hours. The heating rate (20 K/min) and maximum annealing temperature was controlled by a Eurotherm controller connected to a thermocouple placed in vicinity of the sample. The temperature of the sample was calibrated beforehand by a two-color CellaTemp pyrometer. A two-dimensional area detector (Perkin Elmer) with a pixel size of 200 by 200 μm^2 was used to record the diffracted x-ray signal. The sample to detector distance was determined by a LaB_6 NIST standard sample and using the software Fit2D [32]. The strain evolution during annealing is obtained by the $\sin^2\psi$ method using the *c*-TiN and *c*-ZrN 200 diffraction peaks, where the residual stress was calculated with elastic constants for TiN (E=570 GPa) [33] and ZrN (E=462 GPa) [34].

Additional annealing experiments for *ex situ* analysis were carried out in the same vacuum chamber at two different annealing temperatures, 900 °C or 1100 °C, for 2 hours. Grazing incidence x-ray diffraction (GIXRD) using Cu Kα radiation with a fixed incident angle of 4° was applied for enhancing the scattering signals from the coating. Detailed

investigation of the sub-layer structure and phase evolution of coatings was performed in a FEI Tecnai G^2 TF 20 UT transmission electron microscope (TEM) operated at 200 kV. Cross-sectional TEM-samples were prepared by mechanical grinding followed by Ar-ion beam milling to electron transparency.

Atom probe tomography (APT) was performed on 30 nm radius sample tips prepared by FIB milling (FEI Helios nanolab 600) using a standard lift out technique [35]. Measurement of the needle shape samples was performed in a local electrode atom probe instrument (Cameca LEAP 3000X-HR) in laser mode with a 200 kHz frequency, 0.5 nJ per pulse energy and a 532 nm wavelength laser. Tips were set at a ground temperature of 60 K and at a controlled evaporation rate of 0.005 ions per pulse. Data reconstruction was performed in IVAS software package with reconstructed parameters calculated from Kingham curves [36] and scanning electron microscope (SEM) images of the tips. The used parameters were: an evaporation field of 40 V/nm, an image compression factor of 1.65, and a field factor between 3.7 and 4.1. Due to resolution limitation of the APT instrument, overlap of Zr^{+3} and TiN^{+2} isotopes leads to composition errors in 1D concentration profiles and proximity histograms along interfaces. To address this, the different layers (TiN and ZrAlN) were carefully isolated from the interfaces and then a peak deconvolution was performed in order to obtain correct compositions.

The mechanical properties and sliding behavior at the micrometric length scale of each coating system were characterized through nanoindentation and scratch tests, respectively. Hardness (H) was tested using a nanoindenter XP (MTS) and applying the continuous stiffness measurement (CSM) technique [37]. Indentations at a maximum penetration depth of 2000 nm into the surface or until reaching the maximum applied load of 650 mN were performed in a square array of 64 imprints (8x8) using a Berkovich diamond tip. The distance between imprints was kept to 50 µm in order to avoid any overlapping

effects. The indenter area was calibrated using fused silica with a well-known elastic modulus, 72 GPa [38]. The hardness was determined by the Oliver and Pharr method [38] and the results presented are averaged from several indents.

Cube-corner indentations were performed on the coating surface at penetration depths of 250, 500, 1000 and 2000 nm. The purpose of these indents was to qualitatively determine the strength and fracture toughness of different multilayer systems. The residual imprints and the fracture mechanism were studied by a LEO 1550 FEG SEM to identify the critical load at which the first damage event appears in the vicinity of the indent.

Sliding-scratch tests were done at nanometer scale with a Berkovich indenter increasing the load linearly to 500 mN during a length of 500 µm on the coating surface using the nanoindenter described above. The scratch tests were conducted at a constant loading rate of 10 $\mu m \cdot s^{-1}$. Cross-sections of the scratched coatings were prepared by FIB and examined by SEM in a dual beam Workstation (Zeiss Neon 40). Platinum (Pt) layers were deposited before ion milling to protect the sample surface. Specimens were milled using a 30 kV/2 nA Ga^{+} ion beam, which was decreased to 500 pA for the final polish.

3. Results

3.1 Microstructure and strain evolution during annealing

Fig. 1 shows bright-field cross-sectional TEM micrographs presenting an overview of two as-deposited samples studied here. The contrast arises mainly from mass differences and diffraction contrast resulting in bright ZrAlN layers while the dark layers are TiN or ZrN. It shows that both coatings exhibit fine-grain microstructures, with a smaller grain size in the ZrAlN sublayers. Due to the difference in deposition rate, the ZrN sublayers (~12 nm) are

slightly thicker than the TiN sublayers which have a thickness of approximately 10 nm. The ZrAlN layers are approximately 5 nm thick. For both samples, the interfaces are sharp between *w*-ZrAlN and *c*-TiN/*c*-ZrN.

Fig. 2 (a, b) shows GIXRD diffractograms of the as-deposited and annealed multilayers, where "s" indicates the substrate signal. The as-deposited *w*-ZrAlN/*c*-TiN coating displays intense *c*-TiN peaks with a weak shoulder (filled dashed curves) corresponding to *w*-ZrAlN (0002) next to the *c*-TiN (111) peak. The lower volume fraction of *w*-ZrAlN contributes to its relatively low diffraction signal. For *w*-ZrAlN/*c*-ZrN, only diffraction signal originating from *c*-ZrN can be resolved, mainly due to overlap of the diffraction signals from *c*-ZrN and *w*-ZrAlN. It is also affected by the relatively poor crystallinity of the ZrAlN sublayers in *w*-ZrAlN/*c*-ZrN (observed by high-resolution (HR) TEM micrographs in Figs. 4-5). After annealing at 1100 °C, the diffraction peak of *w*-ZrAlN (0002) has shifted to higher angle in *w*-ZrAlN/*c*-TiN coating, resulting in a larger overlap with *c*-TiN 111. For *w*-ZrAlN/*c*-ZrN, a shift of *c*-ZrN diffraction peaks to higher angle is observed after annealed. Also, the width of the diffraction peaks decreases after annealing, which can be related with the growth of *c*-ZrN grains [39].

The selected area electron diffraction patterns (SAED) of the as-deposited coatings are shown in Fig. 2 (c, d). For *w*-ZrAlN/*c*-TiN, *c*-TiN appears slightly textured while *w*-ZrAlN is more textured with (0002) along the growth direction; (10-10) and (11-20) are found in the in-plane directions. For *w*-ZrAlN/*c*-ZrN, the weak signal from *w*-ZrAlN is not clearly distinguishable due to overlapping with *c*-ZrN (111); however, it can be extracted by examination of one-dimensional line profiles obtained by integration of the SAED patterns (also done to resolve the overlapping of *w*-ZrAlN (0002) with *c*-TiN (111)). *c*-ZrN is more randomly oriented compared to *c*-TiN.

Fig. 2 (c, d) also shows SAED patterns from the multilayers after being annealed at 1100 °C for 2 hours. After annealing of the *w*-ZrAlN/*c*-TiN coating, the *w*-ZrAlN (0002) reflection moves to higher angles and approaches the *c*-TiN (111) signal, indicating a decrease of the *w*-ZrAlN (0002) spacing. Table 1 summarizes the lattice spacing of all phases detected by SAED using the d-spacing of *c*-TiN or *c*-ZrN extracted by x-ray diffractometry as reference values. During annealing, the lattice parameters decrease slightly for the *w*-ZrAlN phase, from a=3.22 Å and c=5.00 Å in the as-deposited state to a=3.15 Å and c=4.96 Å in the *w*-ZrAlN/*c*-TiN multilayer. For the *w*-ZrAlN/*c*-ZrN multilayers, the recorded d-spacing of *w*-ZrAlN (10-10) remains similar values. However, due to large degree of overlap the peak deconvolution and lattice parameter determination is less precise in this case. The only change for *w*-ZrAlN/*c*-ZrN during annealing is that the reflections from *c*-ZrN move to higher two-theta values after annealing, which can be related to annihilation of point defects (interstitial or substitutional) frequently observed during annealing of arc deposited coatings [19, 40]. The annihilation should also affect the lattice parameters of *c*-TiN. However, the effect of Zr diffusion into *c*-TiN may counteract the expected lattice spacing decrease.

Fig. 3 shows APT results from the as-deposited and annealed *w*-ZrAlN/*c*-TiN coatings. In the as-deposited state, the proxigram (Fig. 3 (a)) shows that a clear segregation between Ti with Al and Zr atoms takes place at the sub-layer interfaces. Also the 2D contour plot in Fig. 3 (b) shows a homogenous distribution of Zr in the ZrAlN layer. After annealing, Al and Ti are still segregated at the sub-layer interfaces (Fig. 3 (c)), while the Zr atoms are redistributed to the layer interfaces. These changes result in an increase of the Al-fraction in the ZrAlN layer. The 2D contour plot in Fig. 3 (d) shows there is less Zr in the original ZrAlN layer and more at the interfaces between sublayers. It indicates that Zr is mainly located at the interfaces between the original ZrAlN and TiN layers after annealing. For *w*-

ZrAlN/*c*-ZrN, analytical TEM and EDS line scans across the sublayer interfaces reveal that no changes in the compositional profile take place during annealing.

The in-plane strain evolution of *c*-TiN and *c*-ZrN from the two multilayers samples, obtained by *in situ* x-ray scattering during annealing, is shown in Fig. 4. Both as-deposited multilayer samples exhibit compressive strain with a slightly higher value in *c*-TiN (*c*-TiN: -0.63%, *c*-ZrN: -0.48%), which correspond to residual stresses of - 3.59 GPa for *c*-TiN and -2.22 GPa for *c*-ZrN. During annealing below the deposition temperature (~400 °C), the strain increases slightly caused by the difference in thermal expansion coefficients between the substrate and coating [41-44]. Between 400 and 1100 °C, the strain relaxes for both coatings, which is likely a result of a decreasing network of defects [11]. For *w*-ZrAlN/*c*-TiN, the strain relaxation continues slowly during isothermal annealing and the strain has decreased to -0.16% after annealing for 2 hours. For *w*-ZrAlN/*c*-ZrN, *c*-ZrN is under tensile strain when reaching 1100 °C, and the strain increases to 0.13% after 2 hours isothermal annealing.

Fig. 5 shows HRTEM micrographs of the *w*-ZrAlN/*c*-TiN multilayers in the as-deposited state and after annealing at 1100 °C, with the fast Fourier transform (FFT) of the micrographs from each layer as insets in the figure. In Fig. 5 (a), the orientation relation of *c*-TiN (111)[1-10]∣∣ *w*-ZrAlN (0001)[11-20] is observed in the as-deposited state. This coherency is thermodynamically the most favorable for *c*-TiN/*w*-AlN interfaces [45]. After annealing at 1100 °C for 2 hours, the interfaces are partially coherent between TiN and ZrAlN sublayers with the same orientation relation as in the as-deposited state. Coherency is not observed in *w*-ZrAlN/*c*-ZrN multilayers, neither in the as-deposited or annealed states by the HRTEM micrographs (Fig. 6). Also the *c*-110∣∣ *w*-10-10 orientation relation was found to be favorable for ZrN/AlN interfaces, while such interfaces are not found in this study. Besides this, less distinct interfaces are observed in *w*-ZrAlN/*c*-ZrN compared to *w*-ZrAlN/*c*-TiN revealing poor crystalline quality of ZrAlN sublayers, which could be resulted from the

lack of coherency with ZrN during growth. During annealing, the thickness of ZrN layer increases, which agrees with the decreasing peak width observed by XRD (Fig. 2).

Table 1 Lattice spacing of *c*-TiN or *c*-ZrN and *w*-ZrAlN in *w*-ZrAlN/*c*-TiN and *w*-ZrAlN/*c*-ZrN multilayers from SAED and XRD under as-deposited and after annealing at 1100 ºC for 2 hours

		Lattice spacing (Å)	
		as-deposited	**1100 ºC, 2 hours**
***w*-ZrAlN/*c*-TiN**	*w*-ZrAlN (10-10)	2.79	2.75
	w-ZrAlN (0002)	2.50	2.48
	w-ZrAlN (11-20)	1.60	1.57
	c-TiN (111)	2.44	2.44
	c-TiN (200)	2.12	2.12
	c-TiN (220)	1.49	1.49
***w*-ZrAlN/*c*-ZrN**	*w*-ZrAlN (10-10)	2.79	2.77
	c-ZrN (111)	2.66	2.63
	c-ZrN (200)	2.29	2.28
	c-ZrN (220)	1.61	1.61

3.2 Evolution of the mechanical response during annealing

Fig. 7 shows the hardness of *w*-ZrAlN/*c*-TiN and *w*-ZrAlN/*c*-ZrN multilayers in the as-deposited state and after annealing at 900 °C and 1100 °C for 2 hours. The hardness of the two as-deposited samples is similar (~30 GPa). After annealing at 900 °C, the hardness increases for both systems and reaches ~32 GPa for *w*-ZrAlN/*c*-TiN multilayer. At 1100 °C, the hardness of *w*-ZrAlN/*c*-TiN is sustained while it drops to ~30 GPa for *w*-ZrAlN/*c*-ZrN.

The resistance to sliding contact and cracking were investigated by nanoscratch and cube-corner indentation. Fig. 8 (a,b) shows the surface viewed by SEM after nano-scratch

tests with increasing load from 0 to 500 mN along the direction indicated by the arrow. The as-deposited and 900 ºC annealed *w*-ZrAlN/*c*-TiN samples display less damage compared to the ones annealed at 1100 ºC. Damage is recorded as single cohesive failure events at sliding loads higher than ~350 mN. For the coating annealed at 1100 ºC these single failure events occur at 300 mN and above 350 mN multiple events are apparent. For the *w*-ZrAlN/*c*-ZrN multilayer, the as-deposited sample displays the first damage at ~300 mN. The samples annealed 900 ºC and 1100 ºC display large decohesion at loads of around 275 mN and 450 mN, respectively.

Magnifications of failure events marked with dashed boxes in Fig. 8 (a,b) in the two multilayers annealed at 1100 °C are presented in Fig. 8 (c, d). Different failure behaviors are seen for the two samples. *w*-ZrAlN/*c*-TiN shows multiple crack events leading to spallation while *w*-ZrAlN/*c*-ZrN displays larger area of coating delamination with large semi-circular cracks, similar to wedging spallation frequently observed in coatings [26, 46, 47]. The different scratch responses of the multilayers are also displayed in their corresponding depth profiles shown in Fig. 8 (e). The sharp depth variations along the scratch should be interpreted as coating failures [48, 49] except for the first 200 µm where the fluctuations are mostly related to surface defects such as macroparticles (confirmed by SEM). Further, the first failure occurs at ~270 mN (L_{c1}) for both coatings. The higher penetration depth in *w*-ZrAlN/*c*-ZrN could indicate more severe damage events occurring during scratch tests compared to *w*-ZrAlN/*c*-TiN. The two coatings display similar friction coefficient during scratching (~0.15 at the maximum scratch loading).

Fig. 9 shows SEM cross-sectional micrographs recorded beneath the most severely damaged surface along the scratch, i.e. at a load of ~500 mN. For the as-deposited state (Fig. 8 (a)), the *w*-ZrAlN/*c*-TiN multilayer shows good interlayer adhesion and there is only a small crack observed near the coating surface (indicated with an arrow). In contrast, *w*-

ZrAlN/*c*-ZrN (Fig. 9 (b)) displays several cracks on both side of the location where the indenter was sliding across the surface. The cracks are long and run parallel to the layer interfaces. After annealing at 1100 °C (Fig. 9(c)), the *w*-ZrAlN/*c*-TiN multilayer present more cracks in comparison with its as-deposited state. In the case of *w*-ZrAlN/*c*-ZrN annealed at 1100 °C (Fig. 9 (d)), the cracks are larger and have propagated through the coating interior to the surface. The cracks present a serrated shape indicating that propagation was affected by the interfaces within the multilayer. Compared with *w*-ZrAlN/*c*-TiN, the *w*-ZrAlN/*c*-ZrN coating is more severely damaged and partly removed by the scratching.

Fig. 10 shows SEM micrographs of residual cube corner indents with a constant penetration depth of 500 nm for the as-deposited and annealed coatings. The coatings display different cracking behavior, which could be related to differences in fracture toughness. For the *w*-ZrAlN/*c*-TiN multilayers, in the as-deposited state, there are no cracks on the surface while pile-ups around the residual imprint are observed. After annealing at 900 °C, more distinct pile-ups are seen. However, cracks do not appear until the specimen was annealed at 1100 °C. For *w*-ZrAlN/*c*-ZrN multilayers, the as-deposited coating also resists crack formation, but indentation cracks start appearing in coatings annealed at 900 °C. The crack length on the surface further increases in the coating annealed at 1100 °C. Also, the pile-up areas are larger compared with *w*-ZrAlN/*c*-TiN multilayers in both as-deposited and annealed conditions.

By varying the penetration depth and the maximum load during indentation, the critical load (P_c) for the first crack to form on the surface in the vicinity of the indent is extracted for the as-deposited and annealed samples. Fig. 11 shows the change in P_c with annealing condition. The critical load (Fig. 11) is ~150 mN lower for *w*-ZrAlN/*c*-ZrN than *w*-ZrAlN/*c*-TiN in the as-deposited state. For both multilayers, the critical load decreases with annealing temperature compared to their as-deposited states. At the same time the hardness

increases, which often leads to a more brittle behavior [50]. However, for *w*-ZrAlN/*c*-TiN coatings, the critical load stays at a value of ~100 mN even after annealing at 900 °C for 2 hours in comparison to ~10 mN, which is the case for *w*-ZrAlN/*c*-ZrN after the same annealing condition. The critical load for surface crack formation is higher in *w*-ZrAlN/*c*-TiN than *w*-ZrAlN/*c*-ZrN for all conditions.

4. Discussion

4.1 Microstructure and strain evolution during annealing

The phase analysis results from XRD, TEM and SAED yields that both as-deposited multilayer coatings contain layers with a solid solution of *w*-ZrAlN (with the same composition) and *c*-TiN or *c*-ZrN respectively. During annealing at 1100 °C, Zr partly diffuses out from the ZrAlN layers and cause the lattice parameters to decrease during annealing of the *w*-ZrAlN/*c*-TiN multilayer. The mixing energy of *w*-ZrAlN is positive [13] and experimental observations have suggested *w*-ZrAlN to be a metastable alloy with a miscibility gap [19]. On the other hand, above 1000 °C *c*-Ti(Zr)N forms a stable solid solution [51, 52]. Thus, the out-diffusion of Zr results in a *c*-Ti(Zr)N phase formation at the original sublayer interfaces when it is being heat-treated. According to APT data, the ZrN-enriched domains at the interface contains less than 10 at.% of Zr. Effectively this doubles the number of sublayers in this multilayer where it is located. The new Ti(Zr)N phase in the *w*-ZrAlN/*c*-TiN multilayer is not homogenously distributed along the interface, as shown in Fig 3 (d). Instead Ti(Zr)N tends to precipitate heterogeneously along the interface causing incomplete Ti(Zr)N-sublayers. In comparison, out-diffusion of Zr to the interfaces in *w*-ZrAlN/*c*-ZrN multilayers results only into growth of ZrN layers.

An additional difference between the two multilayers is the high degree of the crystallographic coherency between sublayers in *w*-ZrAlN/*c*-TiN for both as-deposited and annealed samples while *w*-ZrAlN/*c*-ZrN displays primarily incoherent sublayer interfaces. It also results in a retained compressive strain in the *c*-TiN sublayers even during annealing while the incoherent *c*-ZrN sublayers are more relaxed in their as-deposited state and exhibit tensile strain when annealed at 1100 °C. In addition, the lattice parameters of *w*-ZrAlN observed in this study (a=3.22 Å and c=5.00 Å) is smaller compared with a single layer w-ZrAlN coating (a=3.25 Å and c=5.2 Å) containing similar Al composition [19]. This is likely a result of the coherency between w-ZrAlN and *c*-TiN/*c*-Ti(Zr)N that leads to compressive strains also in the w-ZrAlN sublayers.

A potential contribution for their difference in coherency can be due to the formation of the interface phase Ti(Zr)N during annealing. Ti(Zr)N has a lower lattice mismatch to both TiN and ZrAlN such that the partial coherency between sublayers is retained even during annealing. In addition, the thermal stability of the interfaces could also play an important role here since the *c*-111| | *w*-0001 type of interfaces has been calculated as the lowest total energy compared with isostructural and heterostructural interfaces for both TiN/AlN and ZrN/AlN multilayer systems [45]. The heterogeneous nature of the Ti(Zr)N-sublayers is expected to cause areas where the coherency is lost during annealing resulting in a lower degree of coherency compared to the as-deposited state.

4.2 Variations in mechanical properties of coatings due to phase changes during annealing

The two multilayers exhibit similar mechanical properties in terms of hardness and surface deformation during scratch resistance in their as-deposited states. However, they display a different cracking behavior where more cracks are generated under the same sliding

load in the *w*-ZrAlN/*c*-ZrN multilayer. Considering the higher thickness for *w*-ZrAlN/*c*-ZrN than *w*-ZrAlN/*c*-TiN, it should result into better scratch resistance of the coating [53, 54]. While the results observed show the opposite, we assign this phenomenon to the combined effect of their differences in elastic mismatch between sublayers and strain state. The effect of elastic mismatch on crack formation under loading is represented by the Dundurs parameter (α) [55], which is given by:

$$\alpha = \frac{E_1 - E_2}{E_1 + E_2} \quad (1)$$

where E_1 and E_2 are the elastic constants of the sublayer materials. α is ~0.32 for *w*-ZrAlN/*c*-TiN and ~0.22 for *w*-ZrAlN/*c*-ZrN system when using an experimental value of the elastic modulus of *w*-ZrAlN [20]. If we use the *ab initio* calculated elastic constant for *w*-ZrAlN [56], α is ~0.50 for *w*-ZrAlN/*c*-TiN and ~0.42 for *w*-ZrAlN/*c*-ZrN. A low Dundurs parameter value indicates a weak sublayer interface, which favors interface cracking [57]. The influence of the sublayer interface strength on crack formation is obvious when comparing the two multilayers before and after annealing where the weak interface *w*-ZrAlN/*c*-ZrN multilayers exhibit crack deflection to a larger extent than the *w*-ZrAlN/*c*-TiN multilayers. In addition, higher compressive strain in as-deposited *c*-TiN than *c*-ZrN should also contribute to better fracture toughness properties since the strain at sub-interfaces in multilayers is shown to affect its mechanical properties [27, 31].

After annealing, both multilayers display higher hardness while it is only sustained in the *w*-ZrAlN/*c*-TiN multilayers after annealing at 1100 °C. The good thermal stability in terms of hardness likely has several origins; the residual stress remains compressive during the entire annealing process, the high degree of coherency across the interfaces and the formation of additional Ti(Zr)N phases at the interface. Further, the Ti(Zr)N phase formation during the annealing process results in a TiN/Ti(Zr)N/(Zr)AlN sublayer structure, where the

additional semi-coherent heterogeneous interfaces at TiN/Ti(Zr)N and Ti(Zr)N/(Zr)AlN contribute to enhanced crack resistance and strength properties [58, 59] compared with incoherent interfaces in *w*-ZrAlN/*c*-ZrN multilayers. Similar enhanced mechanical properties in multilayers with the aid of the secondary phase formed during annealing is also observed for lower Al-content $Zr_{65}Al_{35}N$/TiN multilayers [30].

In the later stages of annealing the *w*-ZrAlN/*c*-ZrN multilayer forms tensile stresses, which promotes more extensive cracking and results in less resistance to failure. Mendibide et al. [27] found that the crack behavior is also affected by the magnitude of the internal stress in the sub-layers where cracks tend to propagate perpendicular to the surface when the stress is low and parallel when the stress is high. The coherency between sublayers is sustained through the annealing in the case of the *w*-ZrAlN/*c*-TiN multilayers, which retains the compressive stress. Thus, the cracks in *w*-ZrAlN/*c*-TiN are running mostly parallel to the coating surface, i.e. along the sub-layer interfaces inside coatings. This is distinctly different compared with *w*-ZrAlN/*c*-ZrN, where the cracks propagate across the sub-layer interfaces all the way to the surface. This results in a higher degree of deformation.

The more extensive crack propagation in *w*-ZrAlN/*c*-ZrN system makes it more prone to surface damage [29] and as a consequence wedge spallation takes place in the annealed state at high load [26, 46, 60]. This is in contrast to the milder damages seen in *w*-ZrAlN/*c*-TiN multilayers caused by cohesive failure, which is also corroborated by its higher resistance to cracking.

5. Conclusion

Arc evaporated *w*-ZrAlN/*c*-TiN and *w*-ZrAlN/*c*-ZrN multilayers are studied with respect to stability of structural and mechanical properties under thermal annealing. Depletion

of Zr from the *w*-ZrAlN sublayers results in formation of the secondary phase Ti(Zr)N in *w*-ZrAlN/*c*-TiN during annealing. The formed phase contributes to a sustained compressive strain during isothermal annealing at 1100 ºC whereas relaxation takes place in *w*-ZrAlN/*c*-TiN. In addition, *w*-ZrAlN sublayers form coherent interfaces with *c*-TiN and the interfaces sustain semi-coherent after 1100 ºC annealing for 2 hours. In contrast, incoherent interfaces in *w*-ZrAlN/*c*-ZrN are found for both as-deposited and annealed states.

These variations in phase and strain evolution strongly affect the hardness and fracture toughness properties. The hardness increase is only retained for *w*-ZrAlN/*c*-TiN multilayers after annealing at 1100 ºC and the resistance to crack propagation is strong. One of the contributions to the phenomenon is the sustained compressive strain. Also, the thermodynamically stable coherent interfaces *c*-TiN (111)| | *w*-ZrAlN (0001) are essential for the strength of interfaces within the sublayers, which presents less damaged coatings under indentations and sliding contact load compared with *w*-ZrAlN/*c*-ZrN.

In summary, the *w*-ZrAlN/*c*-TiN multilayer exhibits superior hardness and crack resistance also after being exposed to elevated temperatures, where the stable, coherent interfaces between *c*-TiN, *c*-Ti(Zr)N and *w*-ZrAlN contribute to enhanced mechanical properties.

Acknowledgment

The EU's Erasmus-Mundus graduate school in Material Science and Engineering (DocMASE), Swedish Research Council VR (621- 2012-4401) and Röntgen-Ångström Cluster grant that includes access to Petra III, Swedish government strategic research area grant AFM – SFO MatLiU (2009-00971), and VINNEX Center of Excellence on Functional

Nanoscale Materials (FunMat) are greatly acknowledged for financial support. We also thank Dr. Naureen Ghafoor for assistance with (S)TEM investigations.

References

[1] H. Holleck, Material selection for hard coatings, Journal of Vacuum Science & Technology A: Vacuum, Surfaces, and Films, 4 (1986) 2661.

[2] N. Norrby, M.P. Johansson, R. M'Saoubi, M. Odén, Pressure and temperature effects on the decomposition of arc evaporated Ti0.6Al0.4N coatings in continuous turning, Surface and Coatings Technology, 209 (2012) 203-207.

[3] P.H. Mayrhofer, C. Mitterer, L. Hultman, H. Clemens, Microstructural design of hard coatings, Prog Mater Sci, 51 (2006) 1032-1114.

[4] P.H. Mayrhofer, M. Stoiber, C. Mitterer, Age hardening of PACVD TiBN thin films, Scripta Materialia, 53 (2005) 241-245.

[5] M. Odén, L. Rogström, A. Knutsson, M.R. Terner, P. Hedström, J. Almer, J. Ilavsky, In situ small-angle x-ray scattering study of nanostructure evolution during decomposition of arc evaporated TiAlN coatings, Applied Physics Letters, 94 (2009) 053114.

[6] A. Knutsson, J. Ullbrand, L. Rogström, N. Norrby, L.J.S. Johnson, L. Hultman, J. Almer, M.P. Johansson Jöesaar, B. Jansson, M. Odén, Microstructure evolution during the isostructural decomposition of TiAlN—A combined in-situ small angle x-ray scattering and phase field study, Journal of Applied Physics, 113 (2013) 213518.

[7] P.H. Mayrhofer, A. Hörling, L. Karlsson, J. Sjölén, T. Larsson, C. Mitterer, L. Hultman, Self-organized nanostructures in the Ti–Al–N system, Applied Physics Letters, 83 (2003) 2049.

[8] R. Rachbauer, S. Massl, E. Stergar, D. Holec, D. Kiener, J. Keckes, J. Patscheider, M. Stiefel, H. Leitner, P.H. Mayrhofer, Decomposition pathways in age hardening of Ti-Al-N films, Journal of Applied Physics, 110 (2011).

[9] N. Norrby, L. Rogström, M.P. Johansson-Jõesaar, N. Schell, M. Odén, In situ X-ray scattering study of the cubic to hexagonal transformation of AlN in Ti1−xAlxN, Acta Materialia, 73 (2014) 205-214.

[10] A. Hörling, L. Hultman, M. Odén, J. Sjölén, L. Karlsson, Mechanical properties and machining performance of Ti1-xAlxN-coated cutting tools, Surface & coatings technology, 191 (2005) 384-392.

[11] D. Rafaja, C. Wustefeld, C. Baehtz, V. Klemm, M. Dopita, M. Motylenko, C. Michotte, M. Kathrein, Effect of Internal Interfaces on Hardness and Thermal Stability of Nanocrystalline Ti0.5Al0.5N Coatings, Metall Mater Trans A, 42a (2011) 559-569.

[12] N. Shulumba, Vibrations in solids : From first principles lattice dynamics to high temperature phase stability, Linköping University Electronic Press, Linköping, 2015, pp. 94.

[13] D. Holec, R. Rachbauer, L. Chen, L. Wang, D. Luef, P.H. Mayrhofer, Phase stability and alloy-related trends in Ti-Al-N, Zr-Al-N and Hf-Al-N systems from first principles, Surface & coatings technology, 206 (2011) 1698-1704.

[14] L. Rogström, M. Ahlgren, J. Almer, L. Hultman, M. Odén, Phase transformations in nanocomposite ZrAlN thin films during annealing, Journal of Materials Research, 27 (2012) 1716-1724.

[15] R. Sanjinés, C.S. Sandu, R. Lamni, F. Lévy, Thermal decomposition of Zr1−xAlxN thin films deposited by magnetron sputtering, Surface and Coatings Technology, 200 (2006) 6308-6312.

[16] P.H. Mayrhofer, D. Sonnleitner, M. Bartosik, D. Holec, Structural and mechanical evolution of reactively and non-reactively sputtered Zr-Al-N thin films during annealing, Surface & coatings technology, 244 (2014) 52-56.

[17] R. Lamni, R. Sanjinés, M. Parlinska-Wojtan, A. Karimi, F. Lévy, Microstructure and nanohardness properties of Zr–Al–N and Zr–Cr–N thin films, Journal of Vacuum Science & Technology A: Vacuum, Surfaces, and Films, 23 (2005) 593.

[18] R. Franz, M. Lechthaler, C. Polzer, C. Mitterer, Oxidation behaviour and tribological properties of arc-evaporated ZrAlN hard coatings, Surface and Coatings Technology, 206 (2012) 2337-2345.

[19] L. Rogström, N. Ghafoor, J. Schroeder, N. Schell, J. Birch, M. Ahlgren, M. Odén, Thermal stability of wurtzite Zr1-xAlxN coatings studied by in situ high-energy x-ray diffraction during annealing, Journal of Applied Physics, 118 (2015).

[20] L. Rogström, M.P. Johansson-Jõesaar, L. Landälv, M. Ahlgren, M. Odén, Wear behavior of ZrAlN coated cutting tools during turning, Surface and Coatings Technology, 282 (2015) 180-187.

[21] A. Knutsson, M.P. Johansson, P.O.A. Persson, L. Hultman, M. Odén, Thermal decomposition products in arc evaporated TiAlN/TiN multilayers, Applied Physics Letters, 93 (2008).

[22] R. Forsén, N. Ghafoor, M. Odèn, Coherency strain engineered decomposition of unstable multilayer alloys for improved thermal stability, Journal of Applied Physics, 114 (2013) 244303

[23] H.C. Barshilia, A. Jain, K.S. Rajam, Structure, hardness and thermal stability of nanolayered TiN/CrN multilayer coatings, Vacuum, 72 (2003) 241-248.

[24] L. Rogström, L.J.S. Johnson, M.P. Johansson, M. Ahlgren, L. Hultman, M. Odén, Thermal stability and mechanical properties of arc evaporated ZrN/ZrAlN multilayers, Thin Solid Films, 519 (2010) 694-699.

[25] A. Knutsson, M.P. Johansson, L. Karlsson, M. Odén, Thermally enhanced mechanical properties of arc evaporated $Ti_{0.34}Al_{0.66}N$/TiN multilayer coatings, Journal of Applied Physics, 108 (2010) 044312.

[26] M. Nordin, M. Larsson, S. Hogmark, Mechanical and tribological properties of multilayered PVD TiN/CrN, Wear, 232 (1999) 221-225.

[27] C. Mendibide, P. Steyer, J. Fontaine, P. Goudeau, Improvement of the tribological behaviour of PVD nanostratified TiN/CrN coatings - An explanation, Surface & coatings technology, 201 (2006) 4119-4124.

[28] K. Yalamanchili, I.C. Schramm, E. Jiménez-Piqué, L. Rogström, F. Mücklich, M. Odén, N. Ghafoor, Tuning hardness and fracture resistance of ZrN/Zr0.63Al0.37N nanoscale multilayers by stress-induced transformation toughening, Acta Materialia, 89 (2015) 22-31.

[29] J.J. Roa, E. Jiménez-Piqué, R. Martínez, G. Ramírez, J.M. Tarragó, R. Rodríguez, L. Llanes, Contact damage and fracture micromechanisms of multilayered TiN/CrN coatings at micro- and nano-length scales, Thin Solid Films, 571 (2014) 308-315.

[30] L. Rogström, N. Ghafoor, M. Ahlgren, M. Odén, Auto-organizing ZrAlN/ZrAlTiN/TiN multilayers, Thin Solid Films, 520 (2012) 6451-6454.

[31] M. Shinn, L. Hultman, S.A. Barnett, Growth, Structure, and Microhardness of Epitaxial Tin/Nbn Superlattices, Journal of Materials Research, 7 (1992) 901-911.

[32] A P Hammersley, `FIT2D: An Introduction and Overview, ESRF Internal Report, ESRF97HA02T, DOI (1997).

[33] F. Tasnadi, I.A. Abrikosov, L. Rogström, J. Almer, M.P. Johansson, M. Odén, Significant elastic anisotropy in Ti1-xAlxN alloys, Applied Physics Letters, 97 (2010).

[34] M.G. Brik, C.G. Ma, First-principles studies of the electronic and elastic properties of metal nitrides XN (X = Sc, Ti, V, Cr, Zr, Nb), Comp Mater Sci, 51 (2012) 380-388.

[35] K. Thompson, D. Lawrence, D.J. Larson, J.D. Olson, T.F. Kelly, B. Gorman, In situ site-specific specimen preparation for atom probe tomography, Ultramicroscopy, 107 (2007) 131-139.

[36] D. Kingham, The post-ionization of field evaporated ions: A theoretical explanation of multiple charge states, Surface Science Letters, 116 (1982) A157.

[37] W.C. Oliver, Measurement of hardness and elastic modulus by instrumented indentation: Advances in understanding and refinements to methodology, DOI (2004).

[38] W.C. Oliver, G.M. Pharr, An Improved Technique for Determining Hardness and Elastic-Modulus Using Load and Displacement Sensing Indentation Experiments, Journal of Materials Research, 7 (1992) 1564-1583.

[39] U.t.G.t. Königliche Gesellschaft der Wissenschaften zu Göttingen, Nachrichten von der Königl. Gesellschaft der Wissenschaften und der G.A. Universität zu Göttingen, Dieterichschen Buchhandlung, Göttingen, 1845.

[40] P.H. Mayrhofer, F. Rovere, M. Moser, C. Strondl, R. Tietema, Thermally induced transitions of CrN thin films, Scripta Materialia, 57 (2007) 249-252.

[41] J.A. Sue, X-ray elastic constants and residual stress of textured titanium nitride coating, Surface and Coatings Technology, 54 (1992) 154-159.

[42] T. Baker, The coefficient of thermal expansion of zirconium nitride, Acta Crystallographica, 11 (1958) 300.

[43] D. Mari, B. Clausen, M.A.M. Bourke, K. Buss, Measurement of residual thermal stress in WC–Co by neutron diffraction, International Journal of Refractory Metals and Hard Materials, 27 (2009) 282-287.

[44] D.S. Rickerby, Internal stress and adherence of titanium nitride coatings, Journal of Vacuum Science & Technology A: Vacuum, Surfaces, and Films, 4 (1986) 2809.

[45] K. Yalamanchili, F. Wang, H. Aboulfadl, J. Barrirero, L. Rogström, E. Jiménez-Pique, F. Mücklich, F. Tasnadi, M. Odén, N. Ghafoor, Growth and thermal stability of TiN/ZrAlN: Effect of internal interfaces, Acta Materialia, 121 (2016) 396-406.

[46] S.J. Bull, Failure mode maps in the thin film scratch adhesion test, Tribol Int, 30 (1997) 491-498.

[47] S.T. Gonczy, N. Randall, An ASTM standard for quantitative scratch adhesion testing of thin, hard ceramic coatings, Int J Appl Ceram Tec, 2 (2005) 422-428.

[48] S.E. Flores, M.G. Pontin, F.W. Zok, Scratching of Elastic/Plastic Materials With Hard Spherical Indenters, J Appl Mech-T Asme, 75 (2008).

[49] S.J. Bull, E.G. Berasetegui, An overview of the potential of quantitative coating adhesion measurement by scratch testing, Tribol Int, 39 (2006) 99-114.

[50] G.R. Anstis, P. Chantikul, B.R. Lawn, D.B. Marshall, A Critical-Evaluation of Indentation Techniques for Measuring Fracture-Toughness .1. Direct Crack Measurements, J Am Ceram Soc, 64 (1981) 533-538.

[51] H. Lind, R. Pilemalm, L. Rogström, F. Tasnadi, N. Ghafoor, R. Forsén, L.J.S. Johnson, M.P. Johansson-Jöesaar, M. Odèn, I.A. Abrikosov, High temperature phase decomposition in TixZryAlzN, Aip Adv, 4 (2014) 127147.

[52] Z.T. Liu, B.P. Burton, S.V. Khare, D. Gall, First-principles phase diagram calculations for the rocksalt-structure quasibinary systems TiN-ZrN, TiN-HfN and ZrN-HfN, J Phys Condens Matter, 29 (2017) 035401.

[53] X. Nie, A. Leyland, H.W. Song, A.L. Yerokhin, S.J. Dowey, A. Matthews, Thickness effects on the mechanical properties of micro-arc discharge oxide coatings on aluminium alloys, Surface and Coatings Technology, 116–119 (1999) 1055-1060.

[54] E. Muzeau, J. von Stebut, B. Magny, The Scratch Resistance of Radiation-Curable Coatings, Metal Finishing, 99 (2001) 21-27.

[55] A.G. Evans, J.W. Hutchinson, The thermomechanical integrity of thin films and multilayers, Acta Metallurgica et Materialia, 43 (1995) 2507-2530.

[56] D. Holec, L. Zhou, H. Riedl, C.M. Koller, P.H. Mayrhofer, M. Friák, M. Šob, F. Körmann, J. Neugebauer, D. Music, M.A. Hartmann, F.D. Fischer, Atomistic Modeling-Based Design of Novel Materials Adv Eng Mater, 19 (2017) 1600688.

[57] S. Suresh, Modeling and design of multi-layered and graded materials, Prog Mater Sci, 42 (1997) 243-251.

[58] I. Salehinia, S. Shao, J. Wang, H.M. Zbib, Plastic Deformation of Metal/Ceramic Nanolayered Composites, Jom-Us, 66 (2014) 2078-2085.

[59] I.N. Mastorakos, H.M. Zbib, D.F. Bahr, Deformation mechanisms and strength in nanoscale multilayer metallic composites with coherent and incoherent interfaces, Applied Physics Letters, 94 (2009).

[60] K. Holmberg, A. Laukkanen, H. Ronkainen, K. Wallin, S. Varjus, J. Koskinen, Tribological contact analysis of a rigid ball sliding on a hard coated surface Part I: Modelling stresses and strains, Surface & coatings technology, 200 (2006) 3793-3809.

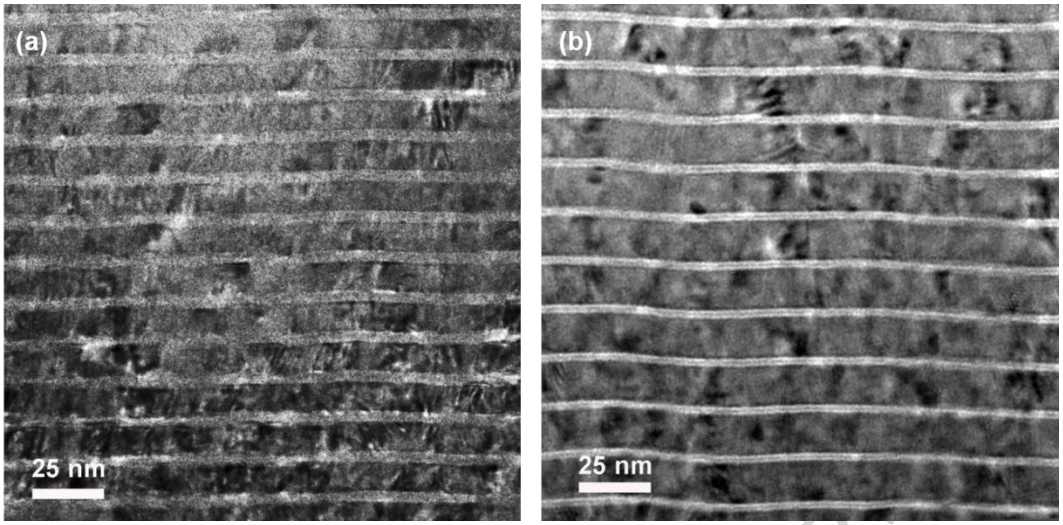

Figure 1 Bright-field TEM of as-deposited (a) *w*-ZrAlN/*c*-TiN and (b) *w*-ZrAlN/*c*-ZrN multilayers

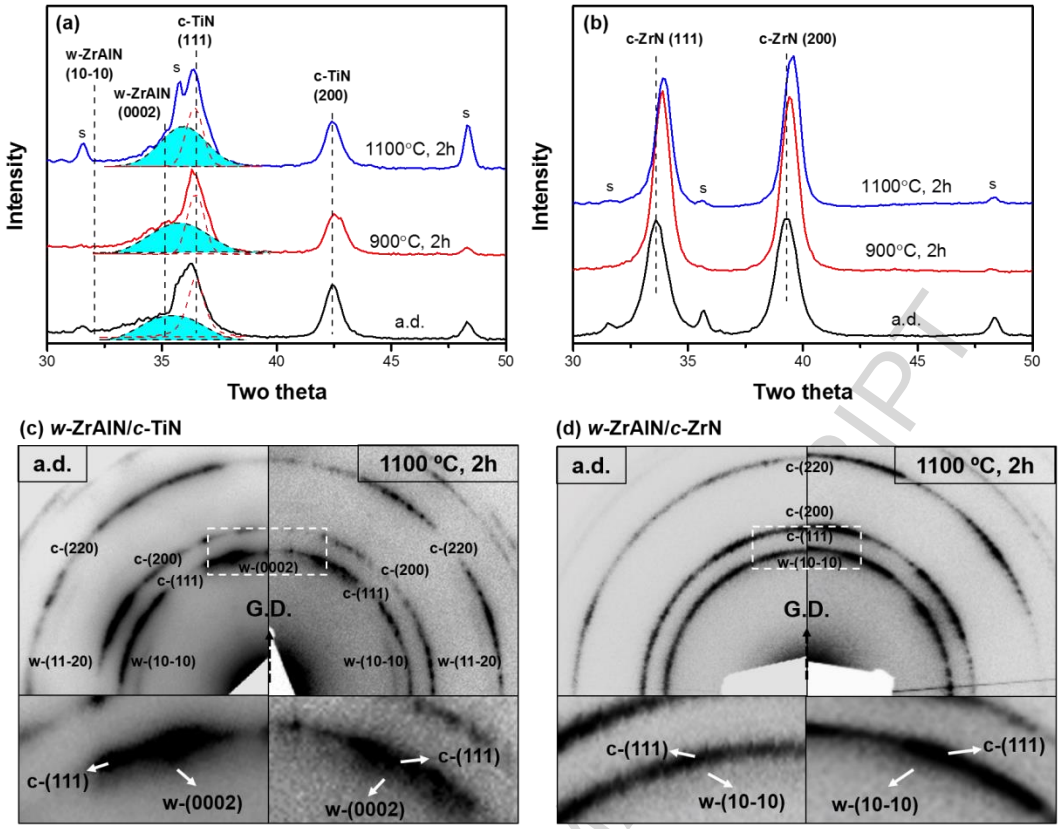

Figure 2 X-ray diffraction results of (a) *w*-ZrAlN/*c*-TiN (dashed filled curves are *w*-ZrAlN (0002), dashed non-filled are *c*-TiN (111)) and (b) *w*-ZrAlN/*c*-ZrN multilayers; SAED patterns of (c) *w*-ZrAlN/*c*-TiN and (d) *w*-ZrAlN/*c*-ZrN multilayers at as-deposited (a.d.) and annealed states. The white dashed squares are magnified as shown below the overall SAED patterns.

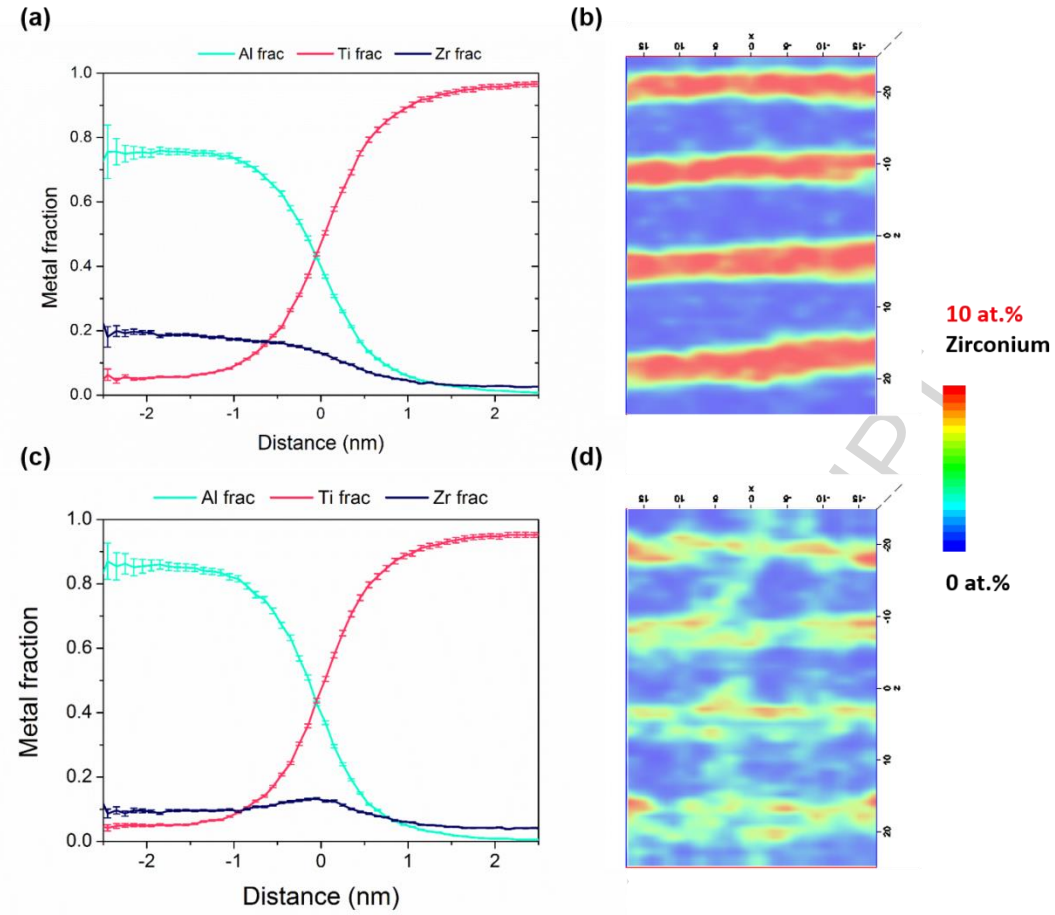

Figure 3 APT proxigrams (a, c) and 2D contour plots (b, d) of *w*-ZrAlN/*c*-TiN multilayers in the as-deposited state (a, b) and after annealing at 1100 °C for 2 hours (c, d).

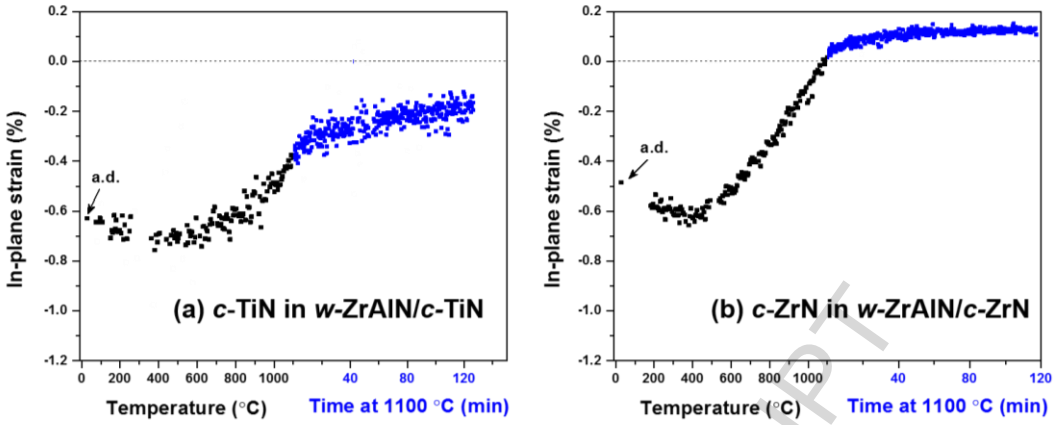

Figure 4 In-plane strain evolution of (a) *c*-TiN in *w*-ZrAlN/*c*-TiN and (b) *c*-ZrN in *w*-ZrAlN/*c*-ZrN multilayers during annealing.

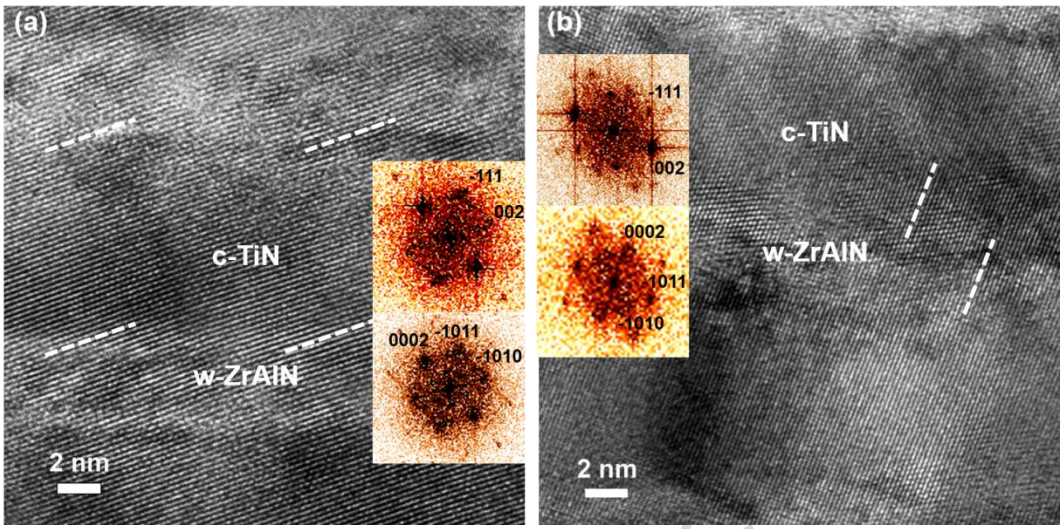

Figure 5 HRTEM micrographs of the *w*-ZrAlN/*c*-TiN multilayer in its (a) as-deposited state and (b) after annealing at 1100 °C for 2 hours, with FFT of two sub-layers with zone axis of c-[110] and w-[10-10].

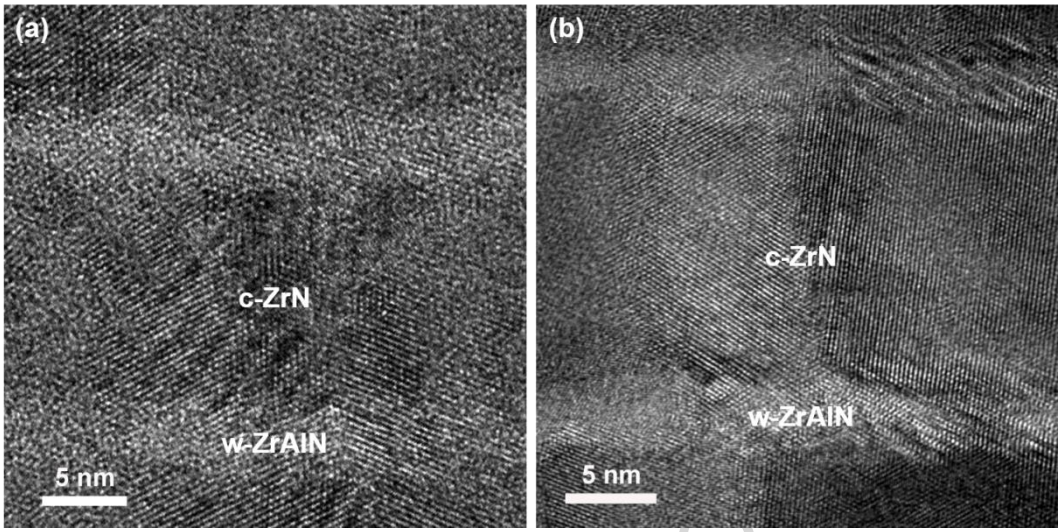

Figure 6 HRTEM micrographs of the *w*-ZrAlN/*c*-ZrN multilayer in its (a) as-deposited state and (b) after annealing at 1100 °C for 2 hours.

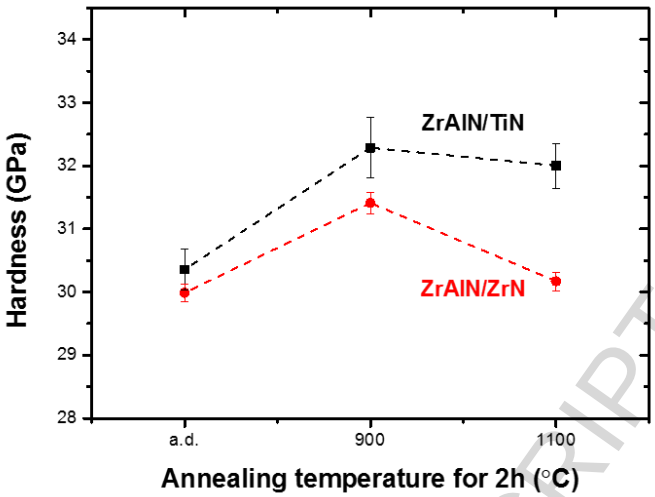

Figure 7 Hardness of *w*-ZrAlN/*c*-TiN (black) and *w*-ZrAlN/*c*-ZrN (red) multilayers in the as-deposited and annealed states.

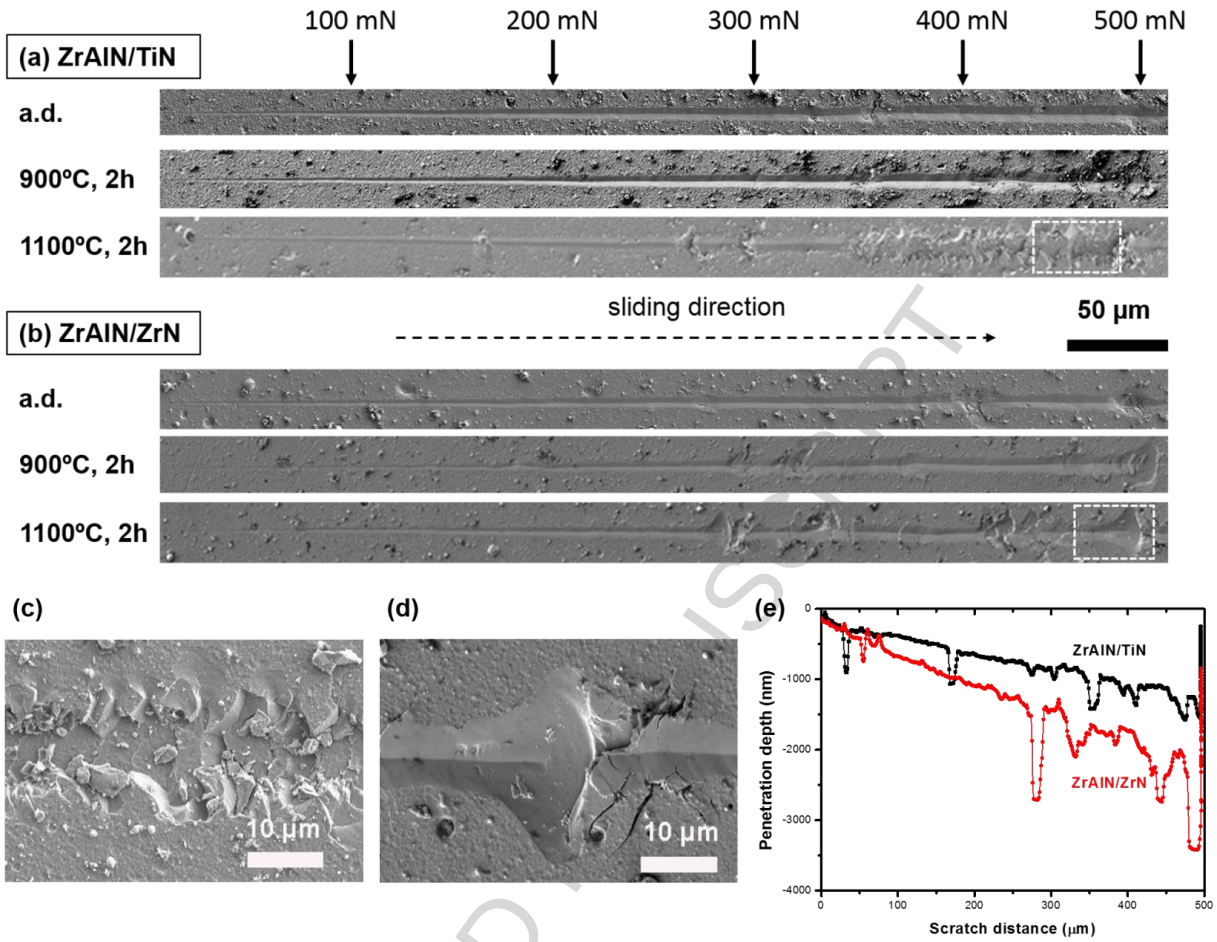

Figure 8 SEM investigation of nano-scratch tracks on (a) *w*-ZrAlN/*c*-TiN and (b) *w*-ZrAlN/*c*-ZrN multilayers under as-deposited, 900 °C and 1100 °C for 2 h; higher resolution images in the dashed box for (c) *w*-ZrAlN/*c*-TiN and (d) *w*-ZrAlN/*c*-ZrN multilayers; (e) Penetration depth during nano-scratch tests for two samples after 1100 °C for 2 h.

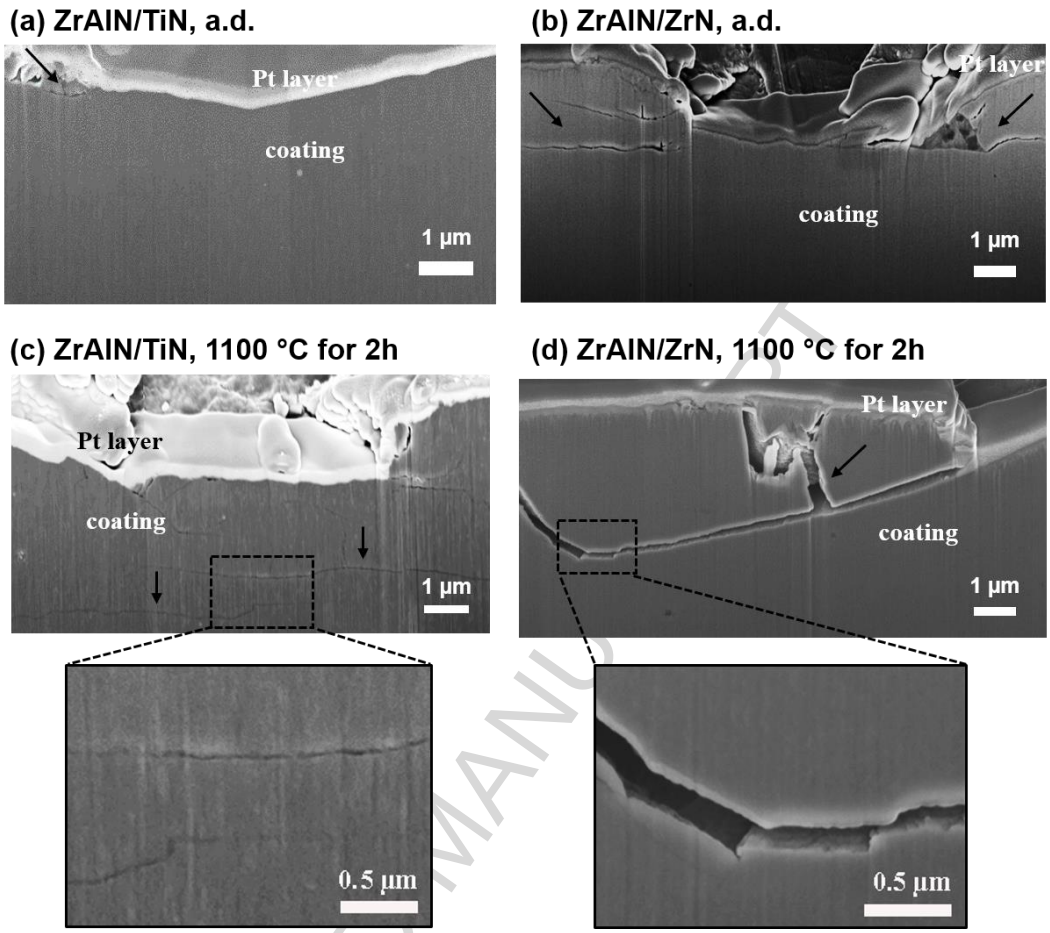

Figure 9 Cross-sections of as-deposited (a, b) and 1100 °C annealing for 2 hours (c, d), with inset of higher resolution on cracks of *w*-ZrAlN/*c*-TiN (a, c) and *w*-ZrAlN/*c*-ZrN multilayers (b, d).

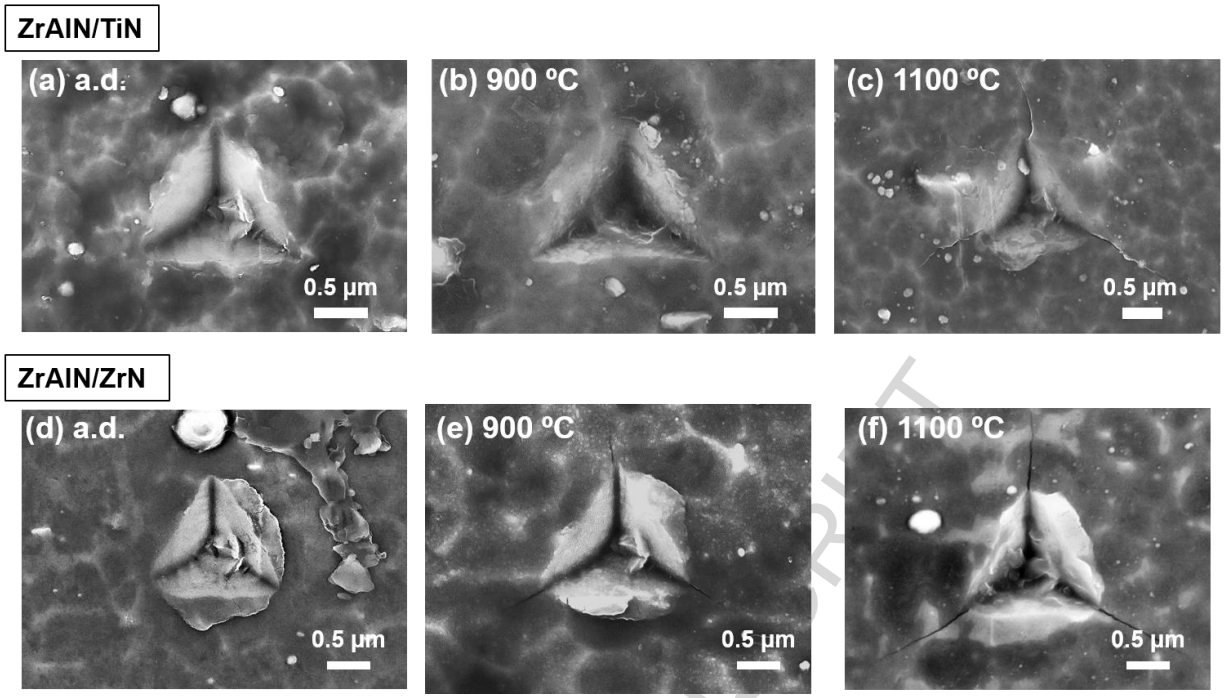

Figure 10 SEM images of imprints from cube-corner indentations on (a-c) *w*-ZrAlN/*c*-TiN and (e-f) *w*-ZrAlN/*c*-ZrN multilayers under as-deposited, 900 °C and 1100 °C for 2 hours under 500 nm penetration depth.

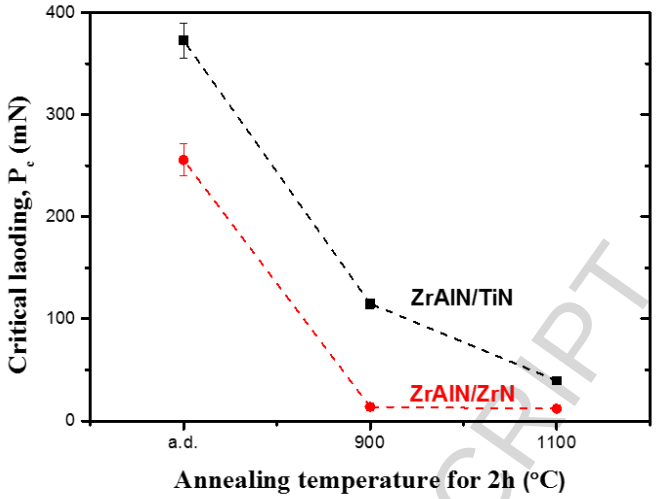

Figure 11 Critical load for forming the first surface crack on *w*-ZrAlN/*c*-TiN (black) and *w*-ZrAlN/*c*-ZrN (red) multilayers coatings in their as-deposited and annealed states.

Highlights

- Coherent interfaces between sublayers are observed for w-ZrAlN/c-TiN multilayers.
- Ti(Zr)N phase formed during annealing at w-ZrAlN/c-TiN interfaces.
- Enhanced mechanical properties of w-ZrAlN/c-TiN coating annealed at 1100 ºC.
- Damages during scratch and indentation are studied related to fracture toughness.